Bioactive Materials 6 (2021) 1365–1374

Contents lists available at ScienceDirect

Bioactive Materials

journal homepage: www.sciencedirect.com/journal/bioactive-materials

A sulfur dioxide polymer prodrug showing combined effect with doxorubicin in combating subcutaneous and metastatic melanoma

Lin An [a], Peng Zhang [b,c], Wei Shen [b], Xuan Yi [b,c], Weitian Yin [a,**], Rihua Jiang [a,***], Chunsheng Xiao [b,c,*]

[a] Department of Hand Surgery and Department of Dermatology, China-Japan Union Hospital of Jilin University, Changchun, 130033, PR China
[b] Key Laboratory of Polymer Ecomaterials, Changchun Institute of Applied Chemistry, Chinese Academy of Sciences, Changchun, 130022, PR China
[c] Jilin Biomedical Polymers Engineering Laboratory, Changchun, 130022, PR China

ARTICLE INFO

Keywords:
Glutathione-responsive
Melanoma
Polymer prodrug
Sulfur dioxide

ABSTRACT

Melanoma, as the most aggressive and treatment-resistant skin malignancy, is responsible for about 80% of all skin cancer mortalities. Prone to invade into the dermis and form distant metastases significantly reduce the patient survival rate. Therefore, early treatment of the melanoma in situ or timely blocking the deterioration of metastases is critical. In this study, a sulfur dioxide (SO_2) polymer prodrug was designed as both an intracellular glutathione (GSH)-responsive SO_2 generator and a carrier of doxorubicin (DOX), and used for the treatment of subcutaneous and metastatic melanoma. Firstly, chemical conjugation of 4-*N*-(2,4-dinitrobenzenesulfonyl)-imino-1-butyric acid (DIBA) onto the side chains of methoxy poly (ethylene glycol) grafted dextran (mPEG-*g*-Dex) resulted in the synthesis of the amphiphilic polymer prodrug of SO_2, mPEG-*g*-Dex (DIBA). The obtained mPEG-*g*-Dex (DIBA) could self-assemble into stable micellar nanoparticles and exhibited a glutathione-responsive SO_2 release behavior. Subsequently, DOX was encapsulated into the core of mPEG-g-Dex (DIBA) micelles to form DOX-loaded nanoparticles (PDDN-DOX). The formed PDDN-DOX could be internalized by B16F10 cells and synchronously release DOX and SO2 into the tumor cells. As a result, PDDN-DOX exerted synergistic anti-tumor effects in B16F10 melanoma cells because of the oxidative damage properties of SO_2 and toxic effects of DOX. Furthermore, *in vivo* experiments verified that PDDN-DOX had great potential for the treatment of subcutaneous and metastasis melanoma. Collectively, our present work demonstrates that the combination of SO_2-based gas therapy and chemotherapeutics offers a new avenue for inhibiting melanoma progression and metastases.

1. Introduction

Melanoma, one of the most lethal skin tumors with prominent morbidity and mortality, has posed a serious threat to human health and identifying effective treatment modalities is of utmost importance [1–3]. In the past few decades, various strategies have been performed for inhibiting the growth and metastasis of melanoma, including immunotherapy using an antibody directed against programmed cell death protein 1 (PD-1). However, more than half of all patients did not respond or only transiently responded to PD-1 blockade [4]. Thus, traditional chemotherapy is still an indispensable strategy for melanoma therapy [5–11]. Especially, the application of nanotechnology to fabricate nanomedicines has made significant contributions to the chemotherapy of melanoma [12–15]. Nanomedicines are equipped with several prominent advantages over small-molecule drugs, including a prolonged blood circulation time and increased accumulation in the tumors because of the enhanced permeability and retention (EPR) effect, which both increases anti-tumor effects and decreases the systemic toxicities of chemotherapeutics [16–21].

Gas therapy refers to the use of gas molecules, such as hydrogen (H_2), hydrogen sulfide (H_2S) and nitric oxide (NO), for treating diseases, which has been recognized as a promising "green treatment" for cancer therapy [22–26]. As a member of the gases family, sulfur dioxide (SO_2) has attracted much attention in inhibiting tumor growth in recent years

* Corresponding author. Key Laboratory of Polymer Ecomaterials, Changchun Institute of Applied Chemistry, Chinese Academy of Sciences, Changchun, 130022, PR China.
** Corresponding author.
*** Corresponding author.
E-mail addresses: yinwt@jlu.edu.cn (W. Yin), jiangrh@jlu.edu.cn (R. Jiang), xiaocs@ciac.ac.cn (C. Xiao).

https://doi.org/10.1016/j.bioactmat.2020.10.027
Received 22 August 2020; Received in revised form 10 October 2020; Accepted 28 October 2020

[27–32]. To achieve controlled and targeted drug release, various stimuli-activated SO_2-releasing nanoplatforms have been prepared for enhanced cancer treatment. For instance, our group developed a glutathione (GSH)-responsive SO_2 polymer prodrug nanovehicle for combating drug-resistance in breast cancer treatment or enhancing the photodynamic therapy via simultaneous depletion of GSH and elevation of reactive oxygen species (ROS) in tumor cells [27,28]. Furthermore, Yang et al. prepared a redox-responsive SO_2-releasing nanoparticle coated with a zwitterionic polymer to achieve increased drug accumulation at the tumor site and subsequently improve cancer treatment [29]. In addition, light-trigged and pH-triggered SO_2-releasing nanoplatforms have also been reported for precise gas or gas-assisted therapy of cancer [30–32]. These studies demonstrated that SO_2 represented a promising therapeutic gas for cancer therapy, and caused apoptosis of cancer cells through the increase of ROS and oxidative damage of intracellular biomacromolecules, such as nuclear DNA.

Herein, a SO_2 polymer prodrug was prepared to release SO_2 in response to intracellular GSH, and was applied as a nanocarrier to load doxorubicin (DOX) for effective treatment of subcutaneous and metastatic melanoma (Scheme 1). The GSH-responsive SO_2-releasing polymer, mPEG-*g*-Dex (DIBA), was prepared by conjugating 4-*N*-(2,4-dinitrobenzenesulfonyl)-imino-1-butyric acid (DIBA) onto the side chains of methoxy poly (ethylene glycol) grafted dextran (mPEG-*g*-Dex). The obtained mPEG-*g*-Dex (DIBA) could self-assemble into micellar nanoparticles (denoted as PDDN) and encapsulate DOX to form DOX-loaded nanoparticles (denoted as PDDN-DOX). PDDN-DOX could be internalized by B16F10 cells and simultaneously release DOX and SO_2 triggered by high GSH levels in the cells (Scheme 1). Additionally, the released SO_2 increased levels of intracellular ROS and exhibited synergistic *in vitro* anticancer effects with DOX by causing oxidative damage to tumor cells. Furthermore, the *in vivo* antitumor efficacy of PDDN-DOX was demonstrated in a subcutaneous and a metastasis melanoma model in mice.

2. Materials and methods

2.1. Materials

Dextran (Dex, M_n = 70 kDa), methoxy poly (ethylene glycol) (mPEG, M_n = 2 kg mol^{-1}), L-glutathione (GSH), γ-aminobutyric acid (GABA), *N*-(3-(dimethylamino)propyl)-*N*-ethylcarbodiimide hydrochloride (EDC·HCl), 4′,6-diamidino-2-phenylindole dihydrochloride (DAPI) and succinic anhydride (ScA) were obtained from Sigma-Aldrich (St. Louis, MI, USA). 4-Dimethylaminopyridine (DMAP), benzoylacetone (BZA), fluorescamine and L-cysteine (Cys) were acquired from Aladdin Bio-Chem Technology Co., Ltd. (Shanghai, China). 2,4-Dinitrobenzenesulfonyl chloride and doxorubicin hydrochloride (DOX·HCl) were acquired from Energy Chemical (Shanghai, China). The fluorescent probe, 7-diethylaminocoumarin-3-aldehyde (DEACA), used for detecting SO_2, was synthesized and characterized according to a previous study [34].

2.2. Cell lines and animals

B16F10 cells were purchased from the Cell Bank of the Chinese Academy of Sciences (Shanghai, China). Female C57BL/6 mice (4–6 weeks, 18–20 g) and female Sprague-Dawley (SD) rats (6–8 weeks, 200–220 g) were obtained from Liaoning Changsheng Biotechnology Ltd. (Liaoning, China). Animals received care according to the Guide for the Care and Use of Laboratory Animals, and all procedures were performed after receiving approval from the Animal Care and Use Committee of Jilin University (Jilin, China).

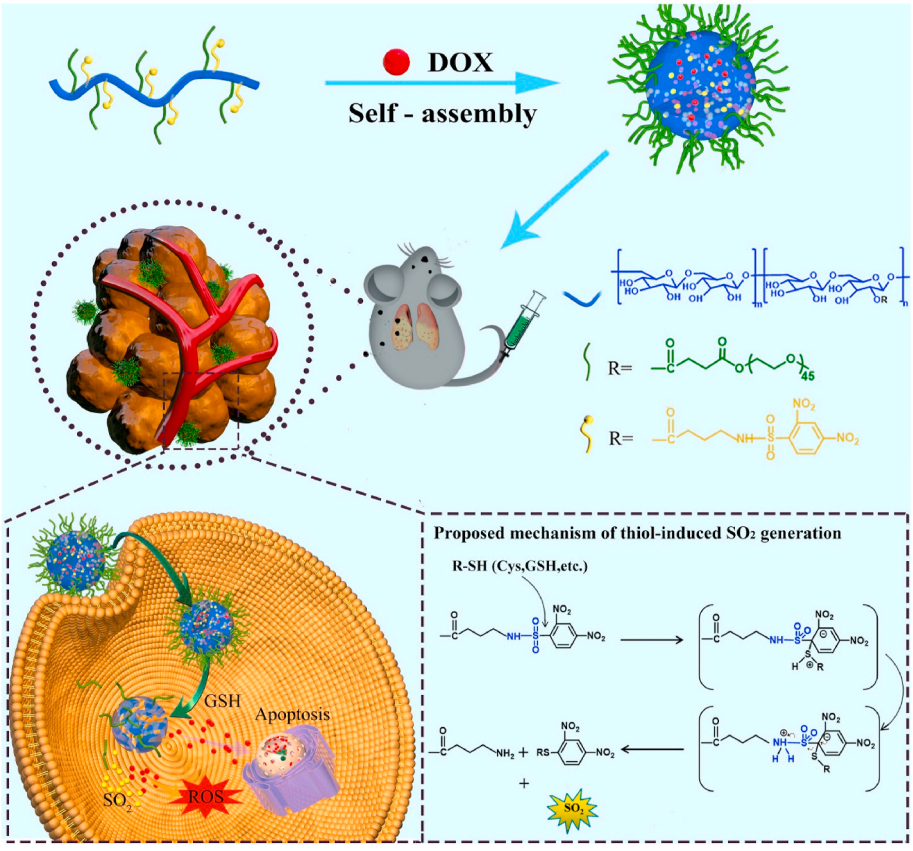

Scheme 1. Schematic illustration of the *in vivo* delivery of doxorubicin-loaded nanoparticles (PDDN-DOX), the GSH-responsive release of DOX and SO_2 in B16F10 cells as well as the possible mechanism for thiol-induced SO_2 generation [33].

2.3. Synthesis

Synthesis of carboxyl terminated mPEG (mPEG-COOH). In brief, mPEG (18.72 g), ScA (5 g), and DMAP (0.48 g) were dissolved in dichloromethane (CH_2Cl_2). The reaction proceeded at room temperature (RT) for 2.5 d. Then, the above solution was precipitated three times in 2 L of ethyl ether to yield the crude product. Finally, mPEG-COOH was obtained after being dried in vacuum (yield: 68.3%). The ^{1}H NMR spectrum (AV-300NMR spectrometer, Bruker, Rheinstetten, Germany) of mPEG-COOH in deuterated chloroform ($CDCl_3$) is presented in Fig. S1A.

Synthesis of mPEG-g-Dex. Dextran (1.62 g) was dissolved in 40 mL dimethyl sulfoxide (DMSO) under ultrasonication for 4.5 h. Subsequently, mPEG-COOH (4.16 g), DMAP (0.12 g), and EDC·HCl (0.38 g) were added and the reaction proceeded at RT for 24 h. Then, the solution was purified (Molecular Weight Cutoff, MWCO 3.5 kDa) with distilled (DI) water, and after lyophilization, mPEG-*g*-Dex was harvested (yield: 52.1%). The ^{1}H NMR spectrum of mPEG-*g*-Dex in deuterated dimethyl sulfoxide (DMSO-d_6) is shown in Fig. S1B.

Synthesis of 4-*N*-(2,4-dinitrobenzenesulfonyl)-imino-1-butyric acid (DIBA). 2,4-Dinitrobenzenesulfonyl chloride (2.71 g) was dissolved in tetrahydrofuran (THF, 40 mL) at 0 °C. Next, GABA (1 g) and sodium hydroxide (NaOH, 0.776 g) in DI water (30 mL) were added dropwise. Subsequently, THF was evaporated and the pH of the residual mixture was adjusted to 1.0 with hydrochloric acid solution. After extraction with CH_2Cl_2, the obtained organic phase was purified with saturated sodium chloride. Then, CH_2Cl_2 was removed, and DIBA was obtained as a yellow solid (yield: 41.6%). The ^{1}H NMR spectrum of DIBA in $CDCl_3$ is presented in Fig. S1C.

Synthesis of mPEG-g-Dex (DIBA). mPEG-*g*-Dex (200 mg), DIBA (28.85 mg), DMAP (12 mg), and EDC·HCl (192 mg) were reacted in DMSO for 24 h. Then, the solution was dialyzed (MWCO 3.5 kDa) with DI water to purify the product. After lyophilization, the mPEG-*g*-Dex (DIBA) was obtained (yield: 64.8%). The ^{1}H NMR spectrum of mPEG-*g*-Dex (DIBA) in DMSO-d_6 is displayed in Fig. S1D.

2.4. Preparation of blank mPEG-g-Dex(DIBA) nanoparticles (PDDN) and DOX-loaded mPEG-g-Dex(DIBA) nanoparticles (PDDN-DOX)

The mPEG-*g*-Dex (DIBA) was dissolved in DMSO and DI water was added dropwise to the solution. After 4 h, the mixture was dialyzed (MWCO 3.5 kDa) with DI water. The self-assembled PDDN was harvested after freeze drying. PDDN-DOX was prepared as follows: mPEG-*g*-Dex (DIBA) and DOX·HCl were dissolved in DMSO, then phosphate buffer saline (PBS, pH = 7.4) was added into the solution. Next, the solution was dialyzed in PBS for 2 h and in DI water for 10 h. PDDN-DOX was obtained as a red solid after lyophilization. The formation of PDDN and PDDN-DOX was verified by dynamic light scattering (DLS) and transmission electron microscopy (TEM). DLS was performed utilizing a Wyatt QELS instrument (DAWN EOS, Wyatt Technology, Goleta, CA, USA). TEM was carried out on a transmission electron microscope (JEM-1011, JEOL, Tokyo, Japan). The drug loading content (DLC) and the drug loading efficiency (DLE) of DOX were measured by a Lambola 365 spectrophotometer (PerkinElmer, San Jose, CA, USA) and calculated using the following formulas:

$$\text{DLC } (wt\ \%) = (\text{weight of loaded DOX/total weight of PDDN-DOX}) \times 100\%$$

$$\text{DLE } (\%) = (\text{weight of loaded DOX/weight of feeding DOX}) \times 100\%$$

2.5. Thiol-responsive property of PDDN

Thiol-induced detachment of 2,4-dinitrobenzenesulfonamide (DNs) groups in the DIBA segment was firstly monitored by ^{1}H NMR spectroscopy using Cys as the triggering molecule. Next, the formation of primary amines after detachment of DNs groups was confirmed by fluorescence spectroscopy using a Fluorescence Master System (Photon Technology International, Birmingham, NJ, USA) using fluorescamine as the probe [35]. Then, the thiol-triggered production of SO_2 was detected using DEACA as the probe. In brief, PDDN was dissolved in PBS (pH = 5.8), then Cys (20 molar equivalents) and DEACA (5 μM) were sequentially added, and the fluorescence intensities of the above-mentioned solutions were measured at preselected times (Photon Technology International, Birmingham, NJ, USA) (λex = 480 nm) [27]. Finally, the GSH-sensitivity of PDDN was demonstrated by measuring changes in the hydrodynamic radius (R_h) in PBS containing 10 mM GSH.

2.6. In vitro release of DOX

In this study, the release behavior of DOX from PDDN-DOX in PBS (pH = 7.4 or 6.5) with different concentrations of GSH was investigated. In brief, the PDDN-DOX solution was placed in a dialysis bag (MWCO 3.5 kDa) in PBS with or without the presence of GSH and shaken at 37 °C. The incubation liquid (2 mL) was withdrawn from the medium and fresh medium was replenished at preselected intervals. The concentration of DOX was determined using a fluorescence spectrometer (λex = 480 nm).

2.7. Cellular uptake

For flow cytometry analysis (FCA), B16F10 cells were cultivated in 6-well plates (3.0×10^5 cells per well) overnight. Free DOX and PDDN-DOX (containing 5 μg mL^{-1} DOX) were separately added into the plates. After culturing for another 3 or 6 h, cells were prepared for flow cytometry (Guava EasyCyte™ 12, Millipore, Burlington, MA, USA). For confocal laser scanning microscopy (CLSM), B16F10 cells were seeded into glass bottom culture dishes (1.0×10^5 cells per well) for 12 h. Next, free DOX and PDDN-DOX (containing 5 μg mL^{-1} DOX) were separately added an incubated for an additional 3 or 6 h. Subsequently, cells were stained with DAPI and visualized by a CLSM (LSM 780, Carl Zeiss, Jena, Germany).

2.8. Determination of SO_2 and ROS level in cells after treatment with PDDN

The release of SO_2 and the generation of ROS in the cells were investigated. First, the B16F10 cells were incubated in the glass-bottomed dishes (5×10^4 cells per well) overnight and then treated with PDDN for another 3 or 6 h. After that, the SO_2 probe DEACA or ROS probe DCFH-DA was added and incubated for 30 min. Then, the B16F10 cells were observed by CLSM. For analysis of ROS level by FCA, B16F10 cells were cultured at a density of 2.0×10^5 cells in a six-well plate for 1 day. Then, the cells were treated with PDDN for 3 or 6 h. DCFH-DA probe was added into the plate and incubated for additional 20 min. After that, the cells were prepared for flow cytometry analysis.

2.9. Cytotoxicity assays

The MTT assay was utilized to evaluate the cytotoxicity of PDDN, free DOX, and PDDN-DOX. In brief, B16F10 cells were cultivated in 96-well plates (5000 cells per well) overnight. Then, cells were incubated with indicated concentrations of the drugs for 48 h or 72 h. Subsequently, the plates were prepared for the MTT assay utilizing a microplate reader (ELX 808, Bio Tek, Winooski, VT, USA) at an absorbance of 490 nm.

2.10. Pharmacokinetics

In this study, SD rats were divided into two groups (n = 3) and received an injection of either free DOX or PDDN-DOX through the tail vein. From each rat, blood was collected from the orbital vein at pre-selected time. Next, blood samples were centrifuged to collect plasma. To measure the serum concentration of DOX, mixtures (150 μL plasma sample, 830 μL methanol, 20 μL daunorubicin hydrochloride) were centrifuged for 10 min. Then, the supernatant was harvested and filtered for high performance liquid chromatography (HPLC) analysis using an E2695 detector (Waters, Boston, MA, USA). The mobile phase consisted of methanol (1600 mL) and an aqueous solution of monopotassium phosphate (KH2PO4) (20 mM, 400 mL). The flow rate was set to 1 mL min^{-1} [36].

2.11. Ex vivo fluorescence imaging

The *ex vivo* fluorescence imaging experiment was performed as follows. First, free DOX or PDDN-DOX was injected intravenously into subcutaneous or metastasis melanoma-bearing mice. After predefined time intervals (3 and 10 h), mice were sacrificed, and tumors and major organs were harvested for fluorescence imaging (Maestro, Cambridge Research & Instrumentation Inc., Woburn, MA, USA).

2.12. In vivo antitumor efficacy

The B16F10 subcutaneous melanoma model was established by subcutaneously inoculation of 1.0×10^6 B16F10 cells into the abdomen. When the melanoma reached about 50 mm^3, mice were grouped and received PBS, PDDN (81.7 mg kg^{-1}), free DOX (3 mg kg^{-1}) or PDDN-DOX (84.7 mg kg^{-1}) through the tail vein on days 0, 3, 6, and 9. Mouse tumor volumes and body weights were recorded every two days. Tumor volumes were calculated as $V = \text{length} \times \text{width}^2/2$. The tumor inhibition rate (%) = $(V_{control}\text{-}V_{sample})/V_{control} \times 100\%$. Herein, $V_{control}$ and V_{sample} represented the average tumor volumes in the control and sample groups, respectively.

The metastatic pulmonary melanoma model was established by an injection of 1×10^5 B16F10 cells per mouse through the tail vein. After five days, mice were randomly grouped and treated with PBS, PDDN (81.7 mg kg^{-1}), free DOX (3 mg kg^{-1}), or PDDN-DOX (84.7 mg kg^{-1}) by tail vein administration. Mice were treated on days 5, 8, 12, and 18 after the implantation of B16F10 cells. On day 27, mice were sacrificed and the treatment effect in the different groups was evaluated.

2.13. Determination of SO_2 and ROS levels in the tumor after treatment with PDDN

The release of SO_2 and generation of ROS in tumor tissue were measured according to the following methods. First, PDDN or PBS was injected intravenously into tumor-bearing mice. After 6 h, mice were sacrificed and tumors were harvested. Then, tumors were prepared for cryo-sections. The obtained tumor slices were stained with the SO_2 probe DEACA or ROS probe DCFH-DA and observed by the CLSM.

2.14. Histological analyses

For histological analysis, major organs and tumors were collected and fixed in buffered formaldehyde (4%). Subsequently, conventional methods were used for embedding and sectioning of the tissues for hematoxylin and eosin (H&E) staining and terminal deoxynucleotidyl transferase mediated dUTP nick-end labeling (TUNEL) analysis [37].

2.15. Statistical analysis

Data were presented as the mean ± standard deviation (SD). Comparisons between groups were analyzed by one-way ANOVA or t tests. $P < 0.05$ was considered statistically significant.

3. Results and discussion

3.1. Synthesis and characterization of mPEG-g-dex (DIBA)

The synthesis route to mPEG-*g*-Dex (DIBA) is illustrated in Scheme S1. First, a small molecule SO_2 prodrug, DIBA, was synthesized by reacting 2,4-dinitrobenzenesulfonyl chloride with γ-aminobutyric acid. The structure of DIBA was characterized by ^{1}H NMR spectrometry (Fig. S1C) and electrospray ionization mass spectrometry (ESI MS) (Fig. S2). Then, the target polymer, mPEG-*g*-Dex (DIBA), was prepared by conjugation of mPEG-COOH and DIBA onto dextran through the formation of ester bonds between a carboxyl group and a hydroxyl group. As shown in Fig. S1D, the ^{1}H NMR spectrum of mPEG-*g*-Dex (DIBA) showed all essential peaks of mPEG, dextran and DIBA, which indicated the successful preparation of mPEG-*g*-Dex (DIBA). Moreover, based on the ^{1}H NMR spectrum, the grafting ratios of mPEG and DIBA were calculated to be 11.3% and 12.8%, respectively.

3.2. Preparation and characterization of PDDN and PDDN-DOX

The resultant mPEG-*g*-Dex (DIBA) could self-assemble into micellar PDDN in aqueous media because of the amphiphilic structure. The critical micelle concentration (CMC) was measured to be 0.0093 mg mL^{-1} using a previously reported method (Fig. S3) [38]. The formation of micellar PDDN was demonstrated by DLS and TEM (Fig. 1A). The R_h of PDDN was 44.4 ± 3.2 nm based on DLS, and TEM indicated that PDDN were spherical in shape with an average size of 66.0 ± 3.1 nm. Next, PDDN were used to encapsulate DOX to form PDDN-DOX. The R_h of PDDN-DOX was determined by DLS and was 51.2 ± 6.1 nm. In addition, the TEM result indicated that the size of PDDN-DOX was 94.7 ± 6.2 nm (Fig. 1B), which was slightly larger than that of PDDN, and was probably due to the loading of DOX. Moreover, the DLC and DLE of DOX in PDDN-DOX were 3.8 wt% and 47.2%, respectively.

3.3. Thiol-response property of PDDN

According to previous studies, the 2,4-dinitrobenzenesulfonamide (DNs) groups could be degraded by thiol compounds to release SO_2, and simultaneously restore the primary amino groups [27,33]. First, the thiol-responsive process of PDDN was observed by time-varied ^{1}H NMR spectra. As presented in Fig. S4, the hydrophobic DIBA segment could not be observed in the initial ^{1}H NMR spectrum of PDDN because it was buried inside the micelle core. However, after adding Cys into the solution, the proton peaks from the DNs group gradually became visible in the ^{1}H NMR spectra with time. Next, the thiol-induced generation of amino groups was evaluated by using fluorescamine as the probe. An obvious increase in fluorescence was observed in the PDDN solution after incubation with 2-mercapto-ethanol (ME) for 2 h, which confirmed the generation of the primary amino group (Fig. 1C). Then, the Cys-induced release of SO_2 was detected with the DEACA fluorescent probe [34]. After adding Cys, the fluorescence intensity of the mixed solution increased along with time in all tested groups (Fig. 1D). The amount of released SO_2 reached ~80% in 2 h (Fig. 1E). The detachment of hydrophobic DNs groups and the formation of hydrophilic amino groups in the side chains caused the transformation of amphiphilic DIBA into hydrophilic polymers, thereby leading to disintegration of PDDN. To verify this property, the thiol-responsive size changes of PDDN in PBS 7.4 were further explored, and the results are displayed in Fig. S5A. After the addition of GSH, the size of PDDN gradually increased over time. Finally, the PDDN disassembled and only irregular aggregates could be observed by TEM (Fig. S5B). Taken together, these data suggested that the prepared PDDN was a type of thiol-responsive nanocarriers with the ability to release SO_2 and the loaded drug in response to thiol-triggering.

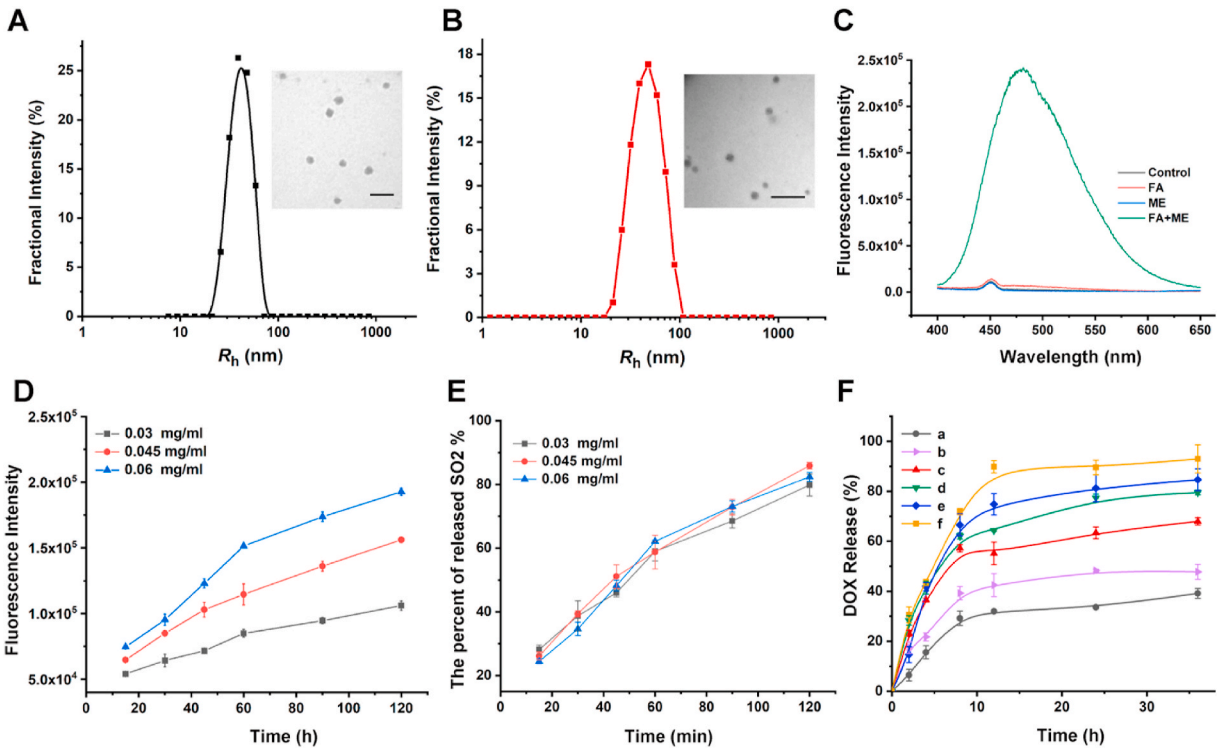

Fig. 1. Dynamic light scattering (DLS) and transmission electron microscopy (TEM) measurement of (A) PDDN (Scale bar: 200 nm) and (B) PDDN-DOX (Scale bar: 500 nm). (C) Free amino group detection in the PDDN group upon treatment with 2-mercapto-ethanol (ME) using a fluorescamine probe. (D) Cys-triggered release of SO_2 from PDDN using DEACA as the fluorescent probe. (E) The calculated released percentages of SO_2 based on the data presented in Fig. 1D. (F) DOX release from PDDN-DOX in PBS: (a) at pH 7.4, (b) at pH 6.5, (c) at pH 7.4 with 5 mM GSH, (d) at pH 6.5 with 5 mM GSH, (e) at pH 7.4 with 10 mM GSH, and (f) at pH 6.5 with 10 mM GSH. Data are presented as the mean ± SD (n = 3).

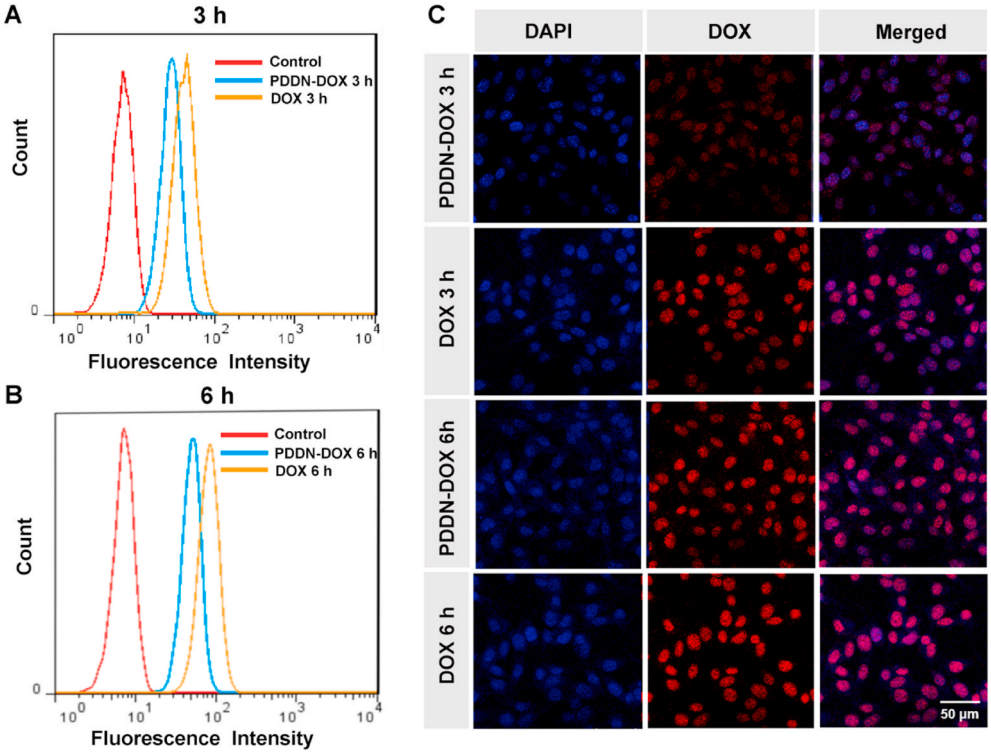

Fig. 2. Flow cytometry analysis (FCA) of B16F10 cells incubated with DOX or PDDN-DOX for 3 h (A) or 6 h (B). (C) CLSM observations of B16F10 cells cultured with DOX or PDDN-DOX for 3 or 6 h.

3.4. In vitro release of DOX

It is well documented that the concentration of GSH in cells (2–10 mM) was much higher compared to that in the extracellular environment (2–20 μM) [39]. Thus, in general, GSH is considered an intracellular trigger that leads to GSH-responsive drug release. In view of the thiol-responsiveness of PDDN, the DOX release behaviors from PDDN-DOX were investigated in PBS (pH = 7.4 or 6.5) with various concentrations of GSH (Fig. 1F). At pH = 7.4, about 40% of DOX was released without the addition of GSH, while 68% and 83% of DOX was released from groups that contained 5 and 10 mM GSH, respectively, after incubation for 36 h. At pH = 6.5, about 48% of DOX was released without the addition of GSH, while 80% and 93% of DOX was released from groups that contained 5 and 10 mM GSH, respectively, after incubation for 36 h. These results confirmed that the release of DOX from PDDN-DOX was GSH-sensitive, which could be ascribed to the GSH-mediated disassociation of PDDN as described above. And the slightly increased release of DOX in acidic conditions was likely due to the protonation of the amino groups of DOX in acidic solutions [36].

3.5. Intracellular release of DOX and SO_2

Cellular internalization of PDDN-DOX was investigated using FCA and CLSM. As shown in Fig. 2A–B and Fig. S6, cells that were incubated with free DOX or PDDN-DOX for 6 h showed a higher fluorescence intensity (FI) compared to cells that were incubated with the same drug formulation for 3 h, which suggested that the uptake of DOX or PDDN-DOX was time-dependent. In addition, the FI in the PDDN-DOX group was weaker compared to that in the free DOX group, likely because the free DOX could more rapidly diffuse into the cells, while PDDN-DOX was internalized by the cells [40,41]. CLSM was also employed to study the endocytosis of DOX and PDDN-DOX by B16F10 cells, and the results were in accordance with the FCA results (Fig. 2C). In summary, the above-mentioned results confirmed that the internalization of PDDN-DOX and release of DOX in B16F10 cells.

The intracellular release of SO_2 was detected by CLSM using DEACA as the probe (Fig. 3A). The control group displayed little blue fluorescence. Comparatively, clear blue fluorescence was observed in the PDDN-treated group, suggesting that SO_2 was released from the PDDN. Furthermore, the FI at 6 h post-treatment was higher compared to that at 3 h post-treatment (Fig. S7), indicating that SO_2 was continuously released from the PDDN. It has previously been reported that intracellularly released SO_2 can increase the level of ROS in cancer cells and subsequently result in cell death [42,43]. Thus, the intracellular ROS level in B16F10 cells was investigated after treatment with PDDN. As shown in Fig. S8A-B, the FI of the PDDN group was higher compared to the control group, which indicated that the production of SO_2 increased the amount of intracellular ROS. In addition, the FI of the 6 h group was higher compared to that of the 3 h group, thereby suggesting that the controlled release of SO_2 and the generation of ROS was time-dependent. These findings were further confirmed by CLSM. PDDN-treated cells showed high green DCF fluorescence and the FI was time-dependent (Fig. 3B and Fig. S9).

3.6. In vitro cytotoxicity assays

The cytotoxicity of the tested formulations was evaluated in B16F10 cells. As shown in Fig. 4, PDDN, DOX, and PDDN-DOX showed dose- and time-dependent inhibition of cell proliferation. PDDN showed effective anti-tumor activity, which indicated that the SO_2-releasing polymer prodrug was efficient in tumor-killing. The anti-tumor mechanism of SO_2 may be ascribed to the oxidative properties of SO_2 as well as its ability to increase intracellular ROS, which induced the death of the tumor cells [25–29]. At an equivalent drug concentration, the order of the cytotoxicity of the tested formulations was as follows: PDDN-DOX > DOX > PDDN. The enhanced cytotoxicity of PDDN-DOX may be ascribed to the synergistic anti-tumor activity of SO_2 and DOX. The calculated combination index (CI) of the released DOX and SO_2 from PDDN-DOX was 0.83 at 48 h and 0.53 at 72 h (CI < 1 representing synergism), respectively. This might be because SO_2 increased intracellular ROS levels, which improved the sensitivity of cancer cells to chemotherapeutic drugs [27,44–48]. Thus, SO_2-enhanced chemotherapy provides a promising method for tumor inhibition.

3.7. Pharmacokinetic analysis

The pharmacokinetics of free DOX and PDDN-DOX were tested in SD rats. Fig. 5 shows that DOX in the PDDN-DOX group maintained a much higher concentration in blood compared to the free DOX group. In addition, the area under the concentration versus time curve from 0 to final time (AUC_{0-t}) of PDDN-DOX was 5.25 mg (mL h)$^{-1}$, which was 18.2-fold that of free DOX. The above-mentioned results confirmed that PDDN-DOX improved the circulation time, which contributed to enhanced drug accumulation in the tumor by the EPR effect.

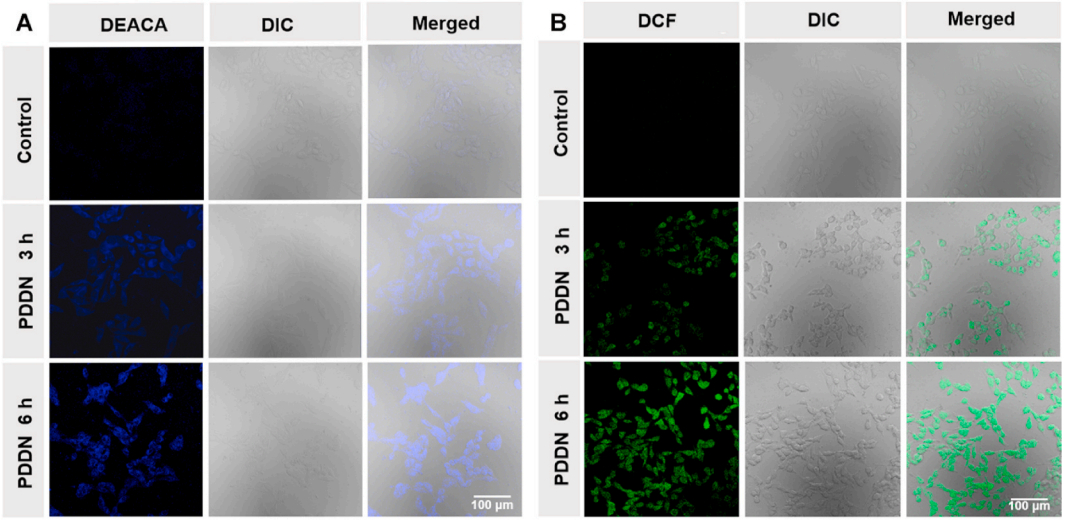

Fig. 3. CLSM images of the intracellular release of SO_2 and ROS, B16F10 cells treated with PDDN for 3 h or 6 h, then stained with DEACA (A) or DCFH-DA (B).

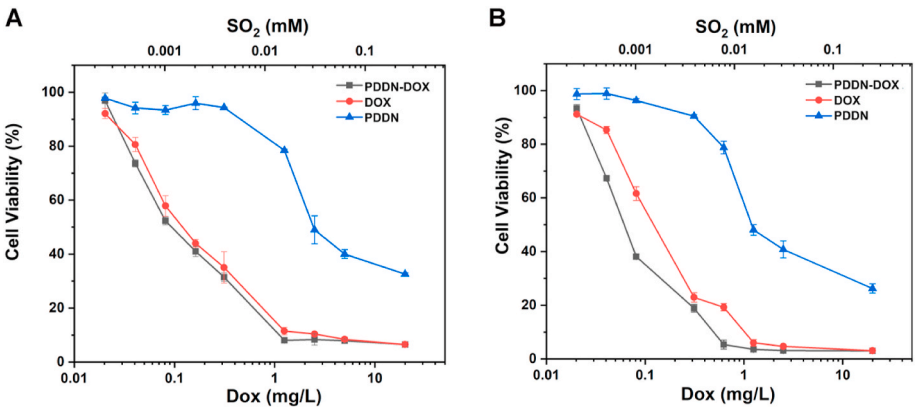

Fig. 4. Viability of B16F10 cells incubated with PDDN, DOX, or PDDN-DOX for 48 h (A) or 72 h (B). Data are presented as the mean ± SD (n = 3).

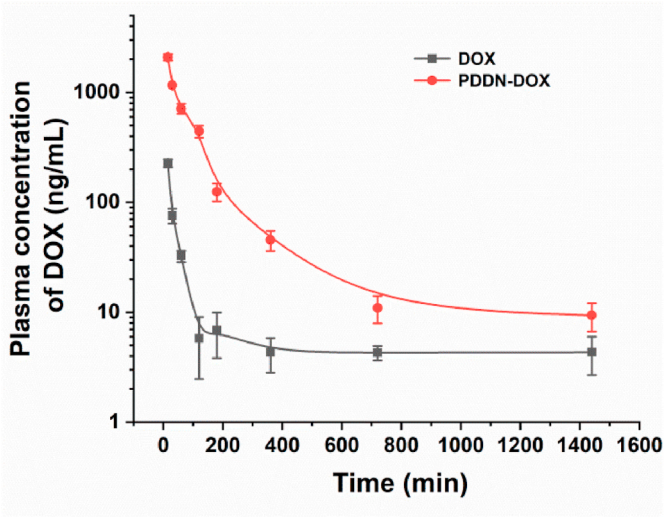

Fig. 5. *In vivo* pharmacokinetics of free DOX and PDDN-DOX. Data are presented as the mean ± SD (n = 3).

3.8. Biodistribution and anticancer efficacy of PDDN-DOX in a subcutaneous melanoma model

Nano-sized PDDN-DOX is expected to highly accumulate in tumor tissue due to the EPR effect [16–21]. To verify this, the biodistribution of PDDN-DOX and free DOX was assessed in mice with subcutaneous xenograft melanoma (Fig. 6A–B). In DOX treated group, the tumor showed visible DOX fluorescence at 3 h, while the fluorescence signal remarkably decreased at 10 h, which indicated the rapid metabolism of DOX. In PDDN-DOX treated group, obvious DOX fluorescence could be observed in tumor site at 3 h and it became stronger at 10 h. In addition, the tumor-to-liver fluorescence ratio (TLFR) was also investigated. As shown in Fig. S10, the TLFR in PDDN-DOX treated group increased with time and was significantly higher than that in DOX treated group at 10 h, indicating the effective accumulation of PDDN-DOX in tumor site, which was consistent with the results in Fig. 6A–B. Taken together, these data suggested that the PDDN-DOX could efficiently accumulate in the tumor because of the EPR effect, which is promising for the treatment of melanoma.

Next, the *in vivo* anti-tumor effect of PDDN-DOX was examined. As presented in Fig. 6C–E, compared with the PBS group, all treatment groups displayed different degrees of tumor suppression. PDDN significantly inhibited tumor growth ($p < 0.001$), which showed that SO_2-releasing nanoparticles were effective for tumor killing *in vivo*. The tumor volumes in the PDDN-DOX group were much smaller compared to those in the free DOX or PDDN group. This could be explained by the combined effect of DOX and SO_2 released from PDDN-DOX. The released DOX could induce cell apoptosis and possible immunogenic cell death [49–52], while the release of SO_2 from PDDN resulted in the increase of ROS levels in tumor site (Fig. S11) and subsequently caused oxidative damages to cancer cells and boosted the antitumor immunity [53–55]. To assess the systemic toxicity of the tested drugs, mouse body weights were recorded during treatment (Fig. 6F). The changes in body weight in the PDDN group and PBS group were similar, indicating little systemic toxicity of PDDN. In addition, less weight loss was observed in the PDDN-DOX group when compared with the free DOX group, which indicated that PDDN-DOX was less toxic than free DOX. This should be ascribed to the fact that PDDN-DOX could protect DOX from leaking in the blood resulting in a higher accumulation at the tumor site via the EPR effect. To further confirm the anticancer effect of PDDN-DOX, H&E staining and TUNEL assay of the tumor tissues were performed (Fig. 6G). Obvious necrosis was observed in the PDDN-, DOX- and PDDN-DOX-treated groups and the largest necrotic area was found in the PDDN-DOX-treated group, indicating that the combination of SO_2 and DOX had an enhanced anticancer effect. In addition, the TUNEL assay showed that PDDN-DOX induced more cell apoptosis compared to free DOX and PDDN. Furthermore, major organs were excised for H&E staining to further evaluate the systemic toxicity of different formulations (Fig. S12). No obvious tissue necrosis was observed in the PDDN-treated groups, indicating little systemic toxicity of PDDN. Specifically, mice exhibited less cardiomyocyte necrosis in the PDDN-DOX group compared to the free DOX group, which implied that PDDN-DOX reduced the systemic side effect. Taken together, these results indicated that PDDN-DOX had great potential for the treatment of melanoma with increased antitumor efficacy and decreased systemic toxicity.

3.9. Biodistribution and anticancer efficacy of PDDN-DOX in a lung metastasis melanoma model

As indicated by the biodistribution of PDDN-DOX in a subcutaneous xenograft melanoma model in mice, PDDN-DOX was prone to accumulate in the lung (Fig. 6A–B). In view of this phenomenon, we anticipated that PDDN-DOX might also be promising for combating lung metastasis melanoma. To test this hypothesis, we firstly re-evaluated the biodistribution of PDDN-DOX in a mouse model of lung metastasis melanoma. As shown in Fig. 7A–B, a stronger fluorescence intensity was observed in the lungs of mice in the PDDN-DOX-treated group compared with mice in the free DOX-treated group at 10 h post-injection, indicating that PDDN-DOX effectively accumulated in metastasis tumors [56,57].

Next, we evaluated the anticancer efficacy of PDDN-DOX in the mouse model of lung metastatic melanoma. The metastatic pulmonary

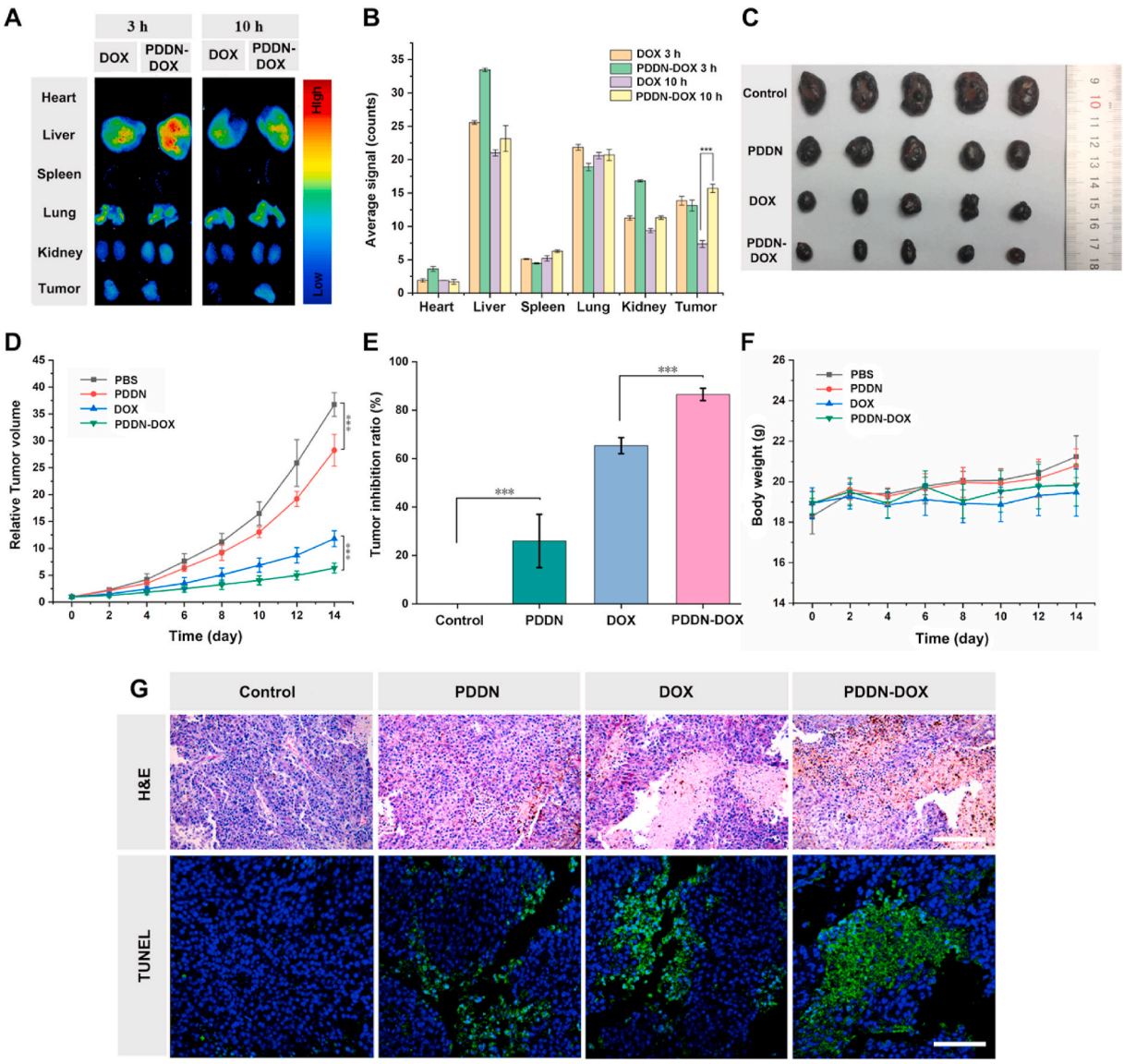

Fig. 6. *In vivo* biodistribution, anticancer efficacy, and toxicity side effects of PDDN-DOX in a B16F10 subcutaneous xenograft tumor model in mice. (A) Biodistribution of free DOX and PDDN-DOX in a B16F10 subcutaneous xenograft tumor model in mice. (B) Average signals of major organs and tumors based on the results in Fig. 6A. (C) Tumor images of various groups on day 14. (D) Changes in tumor volume in mice in different groups (***$p < 0.001$). (E) Tumor inhibition rates of different groups (***$p < 0.001$). (F) Changes in body weight during the treatment course. (G) H&E staining and TUNEL analyses of tumors (Scale bar: 100 μm). Data are presented as the mean ± SD (n = 5).

melanoma model was established by intravenously injecting B16F10 cells (1×10^5 cells per mouse). Five days later, mice were randomly divided into four groups and received PBS, PDDN, free DOX or PDDN-DOX by tail vein administration (Fig. 7C). On day 27, mice were sacrificed and the lungs were harvested. Fig. 7D shows a mass of melanoma metastasized lesions in the PBS-treated group. In contrast, a significantly reduced amount of metastatic nodes was observed in mice treated with PDDN, DOX, or PDDN-DOX. Moreover, the weight of the lungs after treatment was recorded to further evaluate the treatment effects of the tested formulations. The average lung weight of mice in the PDDN-treated group (410.8 ± 66 mg) was almost the half of that of the PBS-treated group (873.2 ± 139.7 mg), implying the SO_2-releasing PDDN was effective for metastatic melanoma treatment (Fig. 7E). Furthermore, mice treated with PDDN-DOX (190.2 ± 9.1 mg) exhibited the lowest average lung weight when compared to either the PDDN-treated group or the free DOX-treated group (242.6 ± 50 mg). The metastatic tumor killing effect of PDDN-DOX was confirmed by H&E staining of the lung tissues (Fig. 7F). Lungs treated with PDDN-DOX showed the lowest infiltration of tumor cells, indicating a better anti-tumor effect of PDDN-DOX compared to the single use of PDDN or free DOX. In addition, mouse body weights were recorded during the treatment. During the first few days, the body weights of mice in the DOX-containing formulations groups were lower compared to those in the PBS and PDDN groups because of the acute drug toxicity. The body weights recovered gradually within 27 days and no significant difference in body weight was observed in all groups at the end of treatment (Fig. S13). Taken together, the above-mentioned results demonstrated that PDDN-DOX was promising for the treatment of in situ melanoma and metastatic pulmonary melanoma.

4. Conclusions

In summary, a GSH-responsive SO_2 polymer prodrug, mPEG-*g*-Dex (DIBA), was successfully prepared and used in combination with DOX

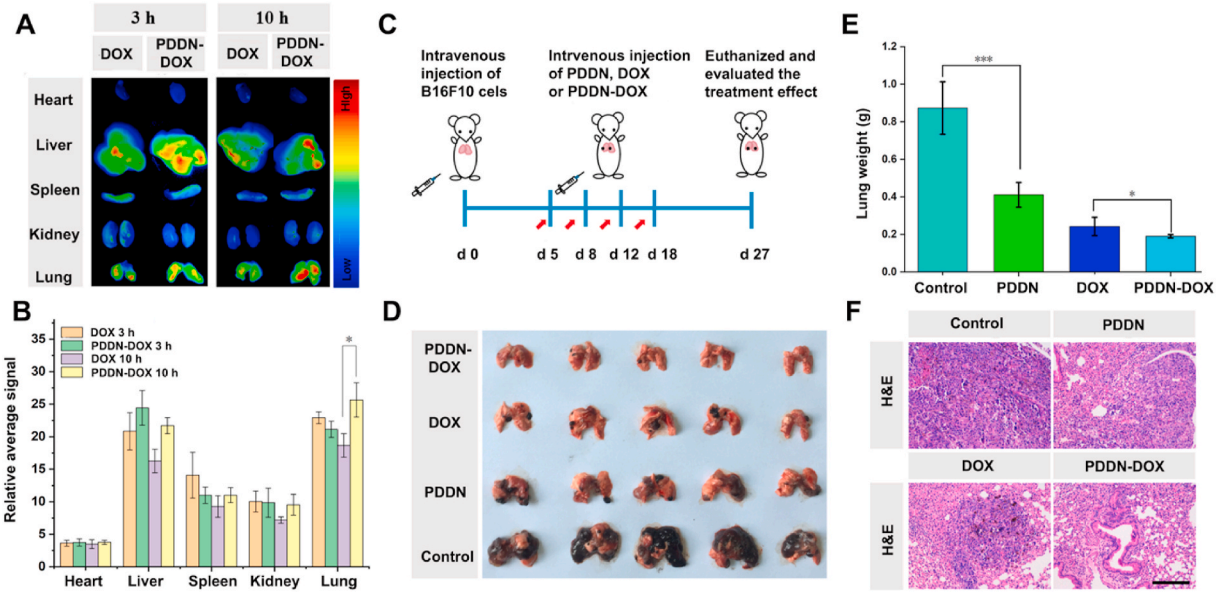

Fig. 7. *In vivo* biodistribution, anticancer efficacy, and toxicity side effects of PDDN-DOX in mice with metastatic lung melanoma. (A) Biodistribution of free DOX or PDDN-DOX in mice with metastatic lung melanoma. (B) Average signals of major organs and lung tumors based on the results in Fig. 7A. (C) Schematic illustration of the experimental procedure. (D) Photographs of lungs excised from mice in different groups on day 27. (E) Average lung weight obtained from mice in different groups on day 27 (*$p < 0.05$, ***$p < 0.001$). (F) Histological sections of lung tissues from different groups. (Scale bar: 100 μm). Data are presented as the mean ± SD (n = 5).

for the treatment of subcutaneous and metastatic melanoma. The mPEG-*g*-Dex (DIBA) could self-assemble into nanoparticles and encapsulate DOX to form a DOX-loaded nanoparticles (PDDN-DOX). The obtained PDDN-DOX could be endocytosed by B16F10 cells and simultaneously released DOX and SO_2 in the cells, thereby inducing a synergistic killing effect of tumor cells *in vitro*. Furthermore, PDDN-DOX exhibited effective anticancer efficacy in the treatment of subcutaneous and metastasis melanoma. The enhanced tumor inhibitory effect of PDDN-DOX should be ascribed to the combined effect of SO_2 and DOX, as well as the EPR effect of nanoparticles. Overall, in the present study, we demonstrated that the use of a SO_2 polymer prodrug as a nanocarrier to efficiently encapsulate chemotherapeutic drugs represented a promising combination strategy (gas therapy and chemotherapy) for the treatment of subcutaneous and metastatic melanoma.

CRediT authorship contribution statement

Lin An: Conceptualization, Investigation, Formal analysis, Writing - original draft. **Peng Zhang:** Writing - review & editing, Funding acquisition. **Wei Shen:** Software analysis, Data curation. **Xuan Yi:** Writing - review & editing. **Weitian Yin:** Conceptualization, Writing - review & editing. **Rihua Jiang:** Conceptualization, Funding acquisition, Supervision. **Chunsheng Xiao:** Conceptualization, Funding acquisition, Writing - review & editing, Supervision.

Declaration of competing interest

The authors declare that they have no competing interest.

Acknowledgements

This study was financially supported by the National Natural Science Foundation of China (51803209, 51773196, and 51573184), the Jilin Provincial Science and Technology Development Program (20190201205JC, 20190103022JH, and 20190103038JH), and the Youth Innovation Promotion Association of Chinese Academy and Sciences (2017266).

Appendix A. Supplementary data

Supplementary data to this article can be found online at https://doi.org/10.1016/j.bioactmat.2020.10.027.

References

[1] D.C. Whiteman, A.C. Green, C.M. Olsen, The growing burden of invasive melanoma: projections of incidence rates and numbers of new cases in six susceptible populations through 2031, J. Invest. Dermatol. 136 (2016) 1161–1171.
[2] H. Mishra, P.K. Mishra, A. Ekielski, M. Jaggi, Z. Iqbal, S. Talegaonkar, Melanoma treatment: from conventional to nanotechnology, J Cancer Res Clin 144 (2018) 2283–2302.
[3] A.E.M. El-Kenawy, C. Constantin, S.M.A. Hassan, A.M. Mostafa, A.F. Neves, T.G. de Araujo, M. Neagu, Nanomedicine in melanoma: current trends and future perspectives, Brisbane (AU), in: W.H. Ward, J.M. Farma (Eds.), Cutaneous Melanoma: Etiology and Therapy, 2017 (Chapter 10).
[4] P. Sharma, S. Hu-Lieskovan, J.A. Wargo, A. Ribas, Primary, adaptive, and acquired resistance to cancer immunotherapy, Cell 168 (2017) 707–723.
[5] F. Rambow, A. Rogiers, O. Marin-Bejar, S. Aibar, J. Femel, M. Dewaele, P. Karras, D. Brown, Y.H. Chang, M. Debiec-Rychter, C. Adriaens, E. Radaelli, P. Wolter, O. Bechter, R. Dummer, M. Levesque, A. Piris, D.T. Frederick, G. Boland, K. T. Flaherty, J. van den Oord, T. Voet, S. Aerts, A.W. Lund, J.C. Marine, Toward minimal residual disease-directed therapy in melanoma, Cell 174 (2018) 843–855.
[6] R.D. Carvajal, C.R. Antonescu, J.D. Wolchok, P.B. Chapman, R.A. Roman, J. Teitcher, K.S. Panageas, K.J. Busam, B. Chmielowski, J. Lutzky, A.C. Pavlick, A. Fusco, L. Cane, N. Takebe, S. Vemula, N. Bouvier, B.C. Bastian, G.K. Schwartz, KIT as a therapeutic target in metastatic melanoma, JAMA, J. Am. Med. Assoc. 305 (2011) 2327–2334.
[7] Y. Cheng, Y. Chang, Y.L. Feng, N. Liu, X.J. Sun, Y.Q. Feng, X. Li, H.Y. Zhang, Simulated sunlight-mediated photodynamic therapy for melanoma skin cancer by titanium-dioxide-nanoparticle-gold-nanocluster-graphene heterogeneous nanocomposites, Small 13 (2017) 1603935.
[8] R.J. Liang, J. Xie, J. Li, K. Wang, L.P. Liu, Y.J. Gao, M. Hussain, G.X. Shen, J.T. Zhu, J. Tao, Liposomes-coated gold nanocages with antigens and adjuvants targeted delivery to dendritic cells for enhancing antitumor immune response, Biomaterials 149 (2017) 41–50.
[9] J.F. Zhou, B. Jin, Y.L. Jin, Y.Z. Liu, J.X. Pan, The antihelminthic drug niclosamide effectively inhibits the malignant phenotypes of uveal melanoma in vitro and in vivo, Theranostics 7 (2017) 1447–1462.
[10] G.S. Karachaliou, F. Ayvali, F.A. Collichio, C.B. Lee, A. Ivanova, D.W. Ollila, S. J. Moschos, Chemotherapy following PD-1 inhibitor blockade in patients with unresectable stage III/stage IV metastatic melanoma: A Single Academic Institution Experience, Oncology (2019) 1–5.
[11] T. Jiang, T. Wang, T. Li, Y. Ma, S. Shen, B. He, R. Mo, Enhanced transdermal drug delivery by transfersome-embedded oligopeptide hydrogel for topical chemotherapy of melanoma, ACS Nano 12 (2018) 9693–9701.

[12] D. Wang, H. Dong, M. Li, Y. Cao, F. Yang, K. Zhang, W. Dai, C. Wang, X. Zhang, Erythrocyte-cancer hybrid membrane camouflaged hollow copper sulfide nanoparticles for prolonged circulation life and homotypic-targeting photothermal/chemotherapy of melanoma, ACS Nano 12 (2018) 5241–5252.

[13] I.V. Zelepukin, A.V. Yaremenko, V.O. Shipunova, A.V. Babenyshev, I.V. Balalaeva, P.I. Nikitin, S.M. Deyev, M.P. Nikitin, Nanoparticle-based drug delivery via RBC-hitchhiking for the inhibition of lung metastases growth, Nanoscale 11 (2019) 1636–1646.

[14] Q.Q. Yu, Y.M. Han, X.C. Wang, C. Qin, D. Zhai, Z.F. Yi, J. Chang, Y. Xiao, C.T. Wu, Copper silicate hollow microspheres-incorporated scaffolds for chemo-photothermal therapy of melanoma and tissue healing, ACS Nano 12 (2018) 2695–2707.

[15] C.N. Zhang, G.N. Shi, J. Zhang, J.F. Niu, P.S. Huang, Z.H. Wang, Y.M. Wang, W. W. Wang, C. Li, D.L. Kong, Redox- and light-responsive alginate nanoparticles as effective drug carriers for combinational anticancer therapy, Nanoscale 9 (2017) 3304–3314.

[16] K. Kataoka, A. Harada, Y. Nagasaki, Block copolymer micelles for drug delivery: design, characterization and biological significance, Adv. Drug Deliv. Rev. 64 (2012) 37–48.

[17] T.M. Sun, Y.S. Zhang, B. Pang, D.C. Hyun, M.X. Yang, Y.N. Xia, Engineered nanoparticles for drug delivery in cancer therapy, Angew. Chem. Int. Ed. 53 (2014) 12320–12364.

[18] R. Sun, N.S. Qiu, Y.Q. Shen, Polymeric cancer nanomedicines: challenge and development, Acta Polym. Sin. 50 (2019) 588–601.

[19] J.J. Shi, P.W. Kantoff, R. Wooster, O.C. Farokhzad, Cancer nanomedicine: progress, challenges and opportunities, Nat. Rev. Canc. 17 (2017) 20–37.

[20] R. Duncan, Polymer conjugates as anticancer nanomedicines, Nat. Rev. Canc. 6 (2006) 688–701.

[21] H. Lian, Y. Du, X. Chen, L. Duan, G. Gao, C. Xiao, X. Zhuang, Core cross-linked poly (ethylene glycol)-graft-Dextran nanoparticles for reduction and pH dual responsive intracellular drug delivery, J. Colloid Interface Sci. 496 (2017) 201–210.

[22] L. Chen, S.F. Zhou, L. Su, J. Song, Gas-mediated cancer bioimaging and therapy, ACS Nano 13 (2019) 10887–10917.

[23] L. Yu, P. Hu, Y. Chen, Gas-generating nanoplatforms: material chemistry, multifunctionality, and gas therapy, Adv. Mater. 30 (2018), e1801964.

[24] Q. He, Precision gas therapy using intelligent nanomedicine, Biomater Sci 5 (2017) 2226–2230.

[25] Y. Wang, T. Yang, Q. He, Strategies for engineering advanced nanomedicines for gas therapy of cancer, National Science Review (2020), https://doi.org/10.1093/nsr/nwaa034.

[26] C. Szabo, Gasotransmitters in cancer: from pathophysiology to experimental therapy, Nat. Rev. Drug Discov. 15 (2016) 185–203.

[27] W. Shen, W. Liu, H. Yang, P. Zhang, C. Xiao, X. Chen, A glutathione-responsive sulfur dioxide polymer prodrug as a nanocarrier for combating drug-resistance in cancer chemotherapy, Biomaterials 178 (2018) 706–719.

[28] Y. Zhang, W. Shen, P. Zhang, L. Chen, C. Xiao, GSH-triggered release of sulfur dioxide gas to regulate redox balance for enhanced photodynamic therapy, Chem. Commun. 56 (2020) 5645–5648.

[29] X. Yao, S. Ma, S. Peng, D. Zhou, R. Xie, Q. Jiang, S. Guo, Q. He, W. Yang, Zwitterionic polymer coating of sulfur dioxide-releasing nanosystem Augments tumor accumulation and treatment efficacy, Adv Healthc Mater 9 (2020), e1901582.

[30] S. Li, R. Liu, X. Jiang, Y. Qiu, X. Song, G. Huang, N. Fu, L. Lin, J. Song, X. Chen, H. Yang, Near-infrared light triggered sulfur dioxide gas therapy of cancer, ACS Nano 13 (2019) 2103–2113.

[31] M. Xu, Q. Lu, Y. Song, L. Yang, J. Li, N. Li, Enhanced Bax upregulating in mitochondria for deep tumor therapy based on SO2 prodrug loaded Au-Ag hollow nanotriangles, Biomaterials 250 (2020) 120076.

[32] Q. Lu, T. Lu, M. Xu, L. Yang, Y. Song, N. Li, SO_2 prodrug doped nanorattles with extra-high drug payload for "collusion inside and outside" photothermal/pH triggered-gas therapy, Biomaterials 257 (2020) 120236.

[33] S.R. Malwal, D. Sriram, P. Yogeeswari, V.B. Konkimalla, H. Chakrapani, Design, synthesis, and evaluation of thiol-activated sources of sulfur dioxide (SO_2) as antimycobacterial agents, J. Med. Chem. 55 (2012) 553–557.

[34] Y. Yang, F. Huo, J. Zhang, Z. Xie, J. Chao, C. Yin, A novel coumarin-based fluorescent probe for selective detection of bisulfite anions in water and sugar samples, Sensor. Actuator. B Chem. 166–167 (2012) 665–670.

[35] S.S. Sidney Udenfriend, Böhlen Peter, Dairman Wallace, Leimgruber Willy, Weigele Manfred, Fluorescamine, A reagent for assay of amino acids, peptides, proteins, and primary amines in the picomole range, Science 178 (1972) 871–872.

[36] H. Yang, W. Shen, W. Liu, L. Chen, P. Zhang, C. Xiao, X. Chen, PEGylated poly (α-lipoic acid) loaded with doxorubicin as a pH and reduction dual responsive nanomedicine for breast cancer therapy, Biomacromolecules 19 (2018) 4492–4503.

[37] P. Zhang, Y. Zhang, X. Ding, C. Xiao, X. Chen, Enhanced nanoparticle accumulation by tumor-acidity-activatable release of sildenafil to induce vasodilation, Biomater Sci 8 (2020) 3052–3062.

[38] A.F. Ana Domínguez, Noemí Gonzalez, Emilia Iglesias, Luis Montenegro, Determination of critical micelle concentration of some surfactants by three techniques, J. Chem. Educ. 74 (1997) 1227.

[39] R. Cheng, F. Feng, F.H. Meng, C. Deng, J. Feijen, Z.Y. Zhong, Glutathione-responsive nano-vehicles as a promising platform for targeted intracellular drug and gene delivery, J. Contr. Release 152 (2011) 2–12.

[40] H. Kawai, Y. Minamiya, M. Kitamura, I. Matsuzaki, M. Hashimoto, H. Suzuki, S. Abo, Direct measurement of doxorubicin concentration in the intact, living single cancer cell during hyperthermia, Cancer-Am Cancer Soc. 79 (1997) 214–219.

[41] G. Sahay, E.V. Batrakova, A.V. Kabanov, Different internalization pathways of polymeric micelles and unimers and their effects on vesicular transport, Bioconjugate Chem. 19 (2008) 2023–2029.

[42] G. Qin, Z. Meng, Effect of sulfur dioxide inhalation on CYP1A1 and CYP1A2 in rat liver and lung, Toxicol. Lett. 160 (2005) 34–42.

[43] B. Poljsak, R. Fink, The protective role of antioxidants in the defence against ROS/RNS-mediated environmental pollution, Oxid. Med. Cell Longev. (2014) 671539.

[44] O. Tredan, C.M. Galmarini, K. Patel, I.F. Tannock, Drug resistance and the solid tumor microenvironment, J. Natl. Cancer Inst. (Bethesda) 99 (2007) 1441–1454.

[45] J.W. Wojtkowiak, D. Verduzco, K.J. Schramm, R.J. Gillies, Drug resistance and cellular adaptation to tumor acidic pH microenvironment, Mol. Pharm. 8 (2011) 2032–2038.

[46] Y. Cai, J. Lu, Z. Miao, L. Lin, J. Ding, Reactive oxygen species contribute to cell killing and P-glycoprotein downregulation by salvicine in multidrug resistant K562/A02 cells, Canc. Biol. Ther. 6 (2007) 1794–1799.

[47] Y.C. Chen, S.R. Bathula, J. Li, L. Huang, Multifunctional nanoparticles delivering small interfering RNA and doxorubicin overcome drug resistance in cancer, J. Biol. Chem. 285 (2010) 22639–22650.

[48] M.Z. Ye, Y.X. Han, J.B. Tang, Y. Piao, X.R. Liu, Z.X. Zhou, J.Q. Gao, J.H. Rao, Y. Q. Shen, A tumor-specific cascade amplification drug release nanoparticle for overcoming multidrug resistance in cancers, Adv. Mater. 29 (2017) 1702342.

[49] J. Fucikova, P. Kralikova, A. Fialova, T. Brtnicky, L. Rob, J. Bartunkova, R. Spisek, Human tumor cells killed by anthracyclines induce a tumor-specific immune response, Canc. Res. 71 (2011) 4821–4833.

[50] R. Kuai, W. Yuan, S. Son, J. Nam, Y. Xu, Y. Fan, A. Schwendeman, J.J. Moon, Elimination of established tumors with nanodisc-based combination chemoimmunotherapy, Sci. Adv. 4 (2018), eaao1736.

[51] Z. Yu, J. Guo, M. Hu, Y. Gao, L. Huang, Icaritin exacerbates mitophagy and synergizes with doxorubicin to induce immunogenic cell death in hepatocellular carcinoma, ACS Nano 14 (2020) 4816–4828.

[52] S. Chen, D. Li, X. Du, X. He, M. Huang, Y. Wang, X. Yang, J. Wang, Carrier-free nanoassembly of doxorubicin prodrug and siRNA for combinationally inducing immunogenic cell death and reversing immunosuppression, Nano Today 35 (2020) 100924.

[53] Y. Lu, Y. Yang, Z. Gu, J. Zhang, H. Song, G. Xiang, C. Yu, Glutathione-depletion mesoporous organosilica nanoparticles as a self-adjuvant and co-delivery platform for enhanced cancer immunotherapy, Biomaterials 175 (2018) 82–92.

[54] S. Ma, W. Song, Y. Xu, X. Si, S. Lv, Y. Zhang, Z. Tang, X. Chen, Rationally designed polymer conjugate for tumor-specific amplification of oxidative stress and boosting antitumor immunity, Nano Lett. 20 (2020) 2514–2521.

[55] H. Deng, Z. Zhou, W. Yang, L.S. Lin, S. Wang, G. Niu, J. Song, X. Chen, Endoplasmic reticulum targeting to amplify immunogenic cell death for cancer immunotherapy, Nano Lett. 20 (2020) 1928–1933.

[56] X.X. Hu, P.P. He, G.B. Qi, Y.J. Gao, Y.X. Lin, C. Yang, P.P. Yang, H. Hao, L. Wang, H. Wang, Transformable nanomaterials as an artificial extracellular matrix for inhibiting tumor invasion and metastasis, ACS Nano 11 (2017) 4086–4096.

[57] Q. Liu, N. Xu, L. Liu, J. Li, Y. Zhang, C. Chen, K. Shezad, L. Zhang, J. Zhu, J. Tao, Dacarbazine-loaded hollow mesoporous silica nanoparticles grafted with folic acid for enhancing antimetastatic melanoma response, ACS Appl. Mater. Interfaces 9 (2017) 21673–21687.